RSC Advances

PAPER

View Article Online
View Journal | View Issue

Cite this: *RSC Adv.*, 2026, **16**, 3950

Electrochemically grown Cu,Ni-BTC film for the electrochemical detection of caffeic acid in fruits

Nguyen Tien Dat,[a] Tran Vinh Hoang,[a] Phan Thi Quyen,[b] Dau Thi Ngoc Nga[c] and Vu Thi Thu *[c]

Caffeic acid (CA) is an important antioxidant often found in many kinds of fruits. In this study, we developed an electrochemical sensor based on an electrochemically grown bimetallic metal–organic framework film (Cu,Ni-BTC) for the *in situ* determination of CA in fruits. The Cu,Ni-BTC film was grown directly onto a glassy carbon electrode (GCE) *via* a cathodic electrodeposition method under optimal conditions. The results showed that a uniform film made of Cu,Ni-BTC metal–organic frameworks with a Cu : Ni molar ratio of 3.67 was grown on the electrode surface. It was found that the charge transfer kinetics were much improved on the electrode modified with the Cu,Ni-BTC material. Consequently, the caffeic acid sensor based on the Cu,Ni-BTC film showed a detection limit and sensitivity as low as 0.7 μM (1.5 times less than that of the unmodified electrode) and 0.924 μA μM^{-1} cm^{-2} (13.2 times higher than that of the unmodified electrode), respectively. The developed sensor also exhibited high reproducibility (RSD = 2.61%), good stability (RSD = 6.47%) after 7 days, and good selectivity towards CA. Real sample tests using apple juice showed good recovery (92.2–98.4%). Further studies will be conducted in the near future to better understand the growth mechanism of the MOF films, control their morphology and utilize them in other electronic applications.

Received 21st October 2025
Accepted 29th December 2025

DOI: 10.1039/d5ra08073h

rsc.li/rsc-advances

1. Introduction

Caffeic acid (CA) (3,4-dihydro-cinnamic acid, $C_9H_8O_4$) is a polyphenol antioxidant found in various plant species (apples and olives), foods (oils), beverages (beer, wine, and pear juice) and some medicines.[1] The mechanism behind the antioxidant behavior of CA is mainly related to the interaction between this molecule and free radicals *via* hydrogen atom transfer and single-electron transfer.[2] CA has shown antiproliferative effects against various cancer cells,[3] bacteria and viruses[4,5] and protective effects against brain-related diseases.[6] For these reasons, CA has been used in skincare products, liver protection products, antioxidant supplements, herbal supplements, medicines,[7] and foodstuffs. Hence, it is essential to develop tools for monitoring CA levels in foods (fresh fruits, beverages and other foods) and other kinds of products. Conventional methods used to detect CA, including high-performance liquid chromatography (HPLC),[8] gas chromatography/mass spectrometry (GC/MS),[9] and capillary electrophoresis,[10] can provide high accuracy, but all of them are time-consuming and expensive and require highly skilled operators.

Electrochemical sensors are a fast and on-site tool for monitoring the level of electroactive compounds such as caffeic acid. Different kinds of materials have been employed to modify the electrode surface in order to improve the electrochemical signals *via* the enhancement of its charge transfer, electrical conductivity or adsorption capacity for the target compound. Conducting polymers such as PEDOT[11] and polydopamine[12] have been utilized to improve the stability and conductivity of sensors. Metal nanoparticles (Au and Ag),[13,14] bimetallic nanostructures (Pt–Ru[15] and Pt–Ni[16]), and oxide particles[17,18] have been widely utilized or combined with other materials to improve electron transfer kinetics and electrical conductivity and possibly introduce electrocatalytic activity. Carbon-based materials[19] and two-dimensional materials[20] have also been demonstrated to be quite effective in improving the performance of sensors for electrochemical CA detection. A common drawback of the above-given sensing materials is their limited adsorption of the target organic compound such as CA due to their rigid nature.

Metal–organic frameworks (MOFs) are crystalline porous materials assembled using metal ions and organic linkers. In recent years, MOFs have gained significant attention due to their high specific surface area, tunable porosity, and abundance of metal active sites,[21,22] despite their low conductivity and stability. Specifically, bimetallic MOFs with mixed-metal centers have been demonstrated to leverage the synergy, thereby enhancing their electrocatalytic performance and

[a]*Hanoi University of Science and Technology (HUST), 1 Dai Co Viet, Bach Mai, Hanoi, Vietnam*

[b]*Hanoi University of Industry (HaUI), 298 Cau Dien, Tay Tuu, Hanoi, Vietnam*

[c]*University of Science and Technology of Hanoi (USTH), Vietnam Academy of Science and Technology (VAST), 18 Hoang Quoc Viet, Nghia Do, Hanoi, Vietnam. E-mail: thuvu.edu86@gmail.com; vu-thi.thu@usth.edu.vn*

stability.[23] Jun *et al.* reported a Ni–Cu bimetallic MOF with high energy density and good stability for energy storage.[24] Several works have demonstrated the use of bimetallic MOF-based sensors for electrochemically detecting phenolic compounds. For example, Gong *et al.* developed a sensing platform using 2D bimetallic Ni/Co MOFs and MWCNTs for dopamine, acetaminophen, and bisphenol A (BPA) detection.[25] Nguyen *et al.* developed a sensing platform for BPA detection using a Cu,Zn-BTC/CNT composite.[26] Huang *et al.* developed a novel bimetallic Ce–Ni-MOF with high sensitivity and a low LOD for BPA determination.[27] Several studies have reported the use of MOFs (GR/CuO@Cu-BTC[28] and NH_2-MIL-101(Fe) nanoparticles[29]) for the electrochemical detection of CA.

Usually, the MOF materials are drop-casted onto the electrode surface, thus limiting their adhesion and increasing the electrode resistance, which are not very beneficial for the sensing performances of the developed electrochemical sensor. Several techniques, such as chemical vapor deposition,[30] liquid-phase epitaxy,[31] and gas ALD/MLD,[32] have been developed to create MOF thin films. The disadvantages of these techniques are their time-consuming nature, high cost and low reproducibility due to complex fabrication processes and expensive instruments.[33] However, MOF thin films fabricated *via* electrochemical methods have much shorter synthesis times and good controllability.[34–36]

In this work, we describe an electrochemical sensing platform with high sensitivity and good selectivity based on a bimetallic MOF (Cu,Ni-BTC) for CA detection. The Cu,Ni-BTC film was electrodeposited on a GCE by chronoamperometry. The presence of an alternative metal center (Ni^{2+}) with good electrocatalytic activity, along with a copper center (Cu^{2+}), might be beneficial for improving the electrical conductivity and electrochemical kinetics at the electrode/electrolyte interface. The porous structure of MOF-based materials should facilitate better adsorption of the target organic compounds onto the electrode surface, as usual, thus improving the recorded electrochemical signals. The morphology, structure and electrochemical behavior of the as-prepared film were investigated, and the correlation between these factors was analyzed to better understand why the electrochemical signals were improved. A new mechanism for the electrochemical oxidation of CA on the MOF-based film was proposed. The performances (calibration curve, repeatability, reproducibility, stability, interference and real sample tests) of the sensing platform were thoroughly tested. The aim of this work was to develop a highly sensitive sensor for *in situ* CA detection in fruits using an electrochemically grown bimetallic metal–organic framework film (Cu,Ni-BTC).

2. Experimental

2.1. Materials

Copper(II) chloride ($CuCl_2 \cdot 2H_2O$), nickel chloride hexahydrate ($NiCl_2 \cdot 6H_2O$), trimesic acid (H_3BTC), *N*,*N*-dimethylformamide (DMF, 98%), potassium ferricyanide ($K_3[Fe(CN)_6]$) and potassium ferrocyanide ($K_4[Fe(CN)_6] \cdot 3H_2O$) were purchased from Sigma-Aldrich and used without further purification. All aqueous solutions were prepared daily with double-distilled water at room temperature. Glassy carbon electrodes (GCEs) (diameter = 3 mm) were used and served as the working electrode for all experiments.

2.2. Electrochemical growth of the Cu,Ni-BTC film on the GCE

Cu,Ni-BTC was synthesized using a cathodic electrodeposition method. The electrodeposition solution was prepared by dissolving 10 mM Et_3N, 15 mM H_3BTC, 9 mM $CuCl_2 \cdot 2H_2O$ and 1 mM $NiCl_2 \cdot 6H_2O$ in a DMF solvent under vigorous stirring for 3 minutes to ensure homogeneity. Before modifying the electrode surface, the GCE was polished with a 0.3-μm Al_2O_3 nanopowder, followed by rinsing thoroughly with ethanol and distilled water and drying at room temperature. The initial investigation of the electrochemical deposition of the Cu,Ni-BTC film was conducted using cyclic voltammetry (CV) in the potential range from −1.5 V to 0 V at a scan rate of 50 mV s^{-1} for 5 cycles. To obtain a more uniform film, chronoamperometry was employed at applied voltages of −0.8 V, −0.9 V, −1 V and −1.1 V (*vs.* Ag/AgCl) for 5 minutes under identical conditions, and the results were compared to identify the optimal growth conditions of the Cu,Ni-BTC film on the GCE, which were then selected for further experiments.

2.3. Morphological and structural characterizations of the electrodeposited Cu,Ni-BTC film

The surface morphology of the samples was examined using field-emission scanning electron microscopy (FE-SEM, JEOL JMS-IT800) at an accelerating voltage of 5 kV. Energy-dispersive X-ray spectroscopy (EDX, JED-2300) was used to identify and quantify the elements present in the samples. X-ray photoelectron spectroscopy (XPS) measurements were performed using a PHI Versa Probe III XPS system employing a monochromatic Al-Kα source at 1486.6 eV. All electrochemical measurements were performed on an Autolab PGSTAT 302N controlled by NOVA 2.0 software equipped with a conventional three-electrode system. The system consisted of a platinum (Pt) auxiliary electrode, an Ag/AgCl/sat. KCl reference electrode, and a bare GCE or modified electrodes as the working electrodes.

2.4. Characterization of the electrochemical behaviors of the electrodeposited Cu,Ni-BTC film

The electrochemical behavior of the bare electrode and modified electrodes was investigated using the cyclic voltammetry (CV) technique in a 0.1 M KCl solution and a 0.1 M KCl solution containing 5 mM $Fe(CN)_6^{3-/4-}$ (conducted separately). To estimate the charge transfer resistance, electrochemical impedance spectroscopy (EIS) measurements were performed in a 0.1 M KCl solution containing 5 mM $Fe(CN)_6^{3-/4-}$ in the frequency range from 10^{-1} to 10^5 Hz.

2.5. Oxidation of caffeic acid on the electrodeposited Cu,Ni-BTC film

The reaction mechanism of CA oxidation on the bare and modified electrodes was investigated by scanning electrodes in a PBS solution (pH 3) containing 500 μM caffeic acid in the

potential window between −400 mV and 1 V at a scan rate of 50 mV s^{-1}. The effect of the scan rate and pH level on the redox behaviors of CA on the GCE and Cu,Ni-BTC/GCE was also evaluated by the CV technique.

2.6. Sensing performances

2.6.1. Calibration curves. For CA detection, differential pulse stripping voltammetry (DPV) measurements were carried out in the solutions containing the desired CA concentration. The DPV parameters were set as follows: a potential range of 300–700 mV, a differential step of 5 mV, a pulse amplitude of 5 V, a pulse width of 0.08 s and a sampling time of 0.04 s. The DPV responses of the electrodeposited Cu,Ni-BTC, Cu-BTC, and Ni-BTC electrodes and bare GCE in PBS (pH 3) containing caffeic acid at different concentrations (2–25 μM) were recorded and analyzed to plot calibration curves.

2.6.2. Stability and reproducibility tests. The reproducibility of the sensor was assessed by recording the DPV curves of seven individual Cu,Ni-BTC/GCE electrodes prepared under the same conditions. The stability of the fabricated Cu,Ni-BTC/GCE was also evaluated over a period of 7 days.

2.6.3. Interference study. The selectivity of Cu,Ni-BTC/GCE toward CA was evaluated by performing an interference study using the DPV technique. The effect of potential interferents on the sensor's performance was evaluated by analyzing the DPV responses of CA in the presence of potential interfering species commonly found in real samples, such as gallic acid (GA), ascorbic acid (AA), and uric acid (UA).

2.6.4. Real sample study. Apples were purchased from a local supermarket in Hanoi, Vietnam, and juiced using a juicer. A 100 mL sample of apple juice was transferred to a centrifuge tube and centrifuged at 4000 rpm to obtain a clear supernatant. The obtained solution (60 mL) was then divided into 6 tubes, spiked with different volumes (0 μL, 0.6 μL, 1.20 μL, 1.5 μL, 2.4 μL, and 3.0 μL) of a standard CA solution (50 μM) and then diluted with PBS (pH = 3) to obtain a final volume of 15 mL for each solution. The mixtures were sonicated for 10 minutes prior to analysis using the DPV technique. By plotting the peak intensity as a function of the concentration and then extrapolating the calibration curve in Origin software, the concentration of CA in the test sample could be determined.

3. Results and discussions

3.1. Electrochemical synthesis process of the Cu,Ni-BTC film

The Cu,Ni-BTC film is electrodeposited on a glassy carbon electrode using the cathodic deposition method. The formation of the Cu,Ni-BTC film begins with the deprotonation of BTC^{3-} ions derived from the H_3BTC organic ligand. This is followed by the coordination of BTC^{3-} with Cu^{2+} and Ni^{2+} ions derived from $CuCl_2 \cdot 2H_2O$ and $NiCl_2 \cdot 6H_2O$, respectively, to form Cu,Ni-BTC crystals. As observed in Fig. S1, a distinct peak corresponding to H^+ reduction at −0.88 V is observed in the first scan cycle. This peak is associated with the deprotonation of the organic ligand *via* the following reaction: $H_3BTC + 3Et_3N \rightarrow BTC^{3-} + 3Et_3NH^+$.[37] In the subsequent cycles, the intensity of this peak decreases due to a local decrease in the concentration of the precursor (H_3BTC) near the electrode surface. Triethylamine (Et_3N) is used as a probase to accelerate the deprotonation of H_3BTC in solution.[38] Other probases, like nitrate (NO_3^-), can be used in the MOF synthesis process; however, they generally demand high reduction overpotentials.[38–40] Simultaneously, under negative potentials, water molecules from hydrated salts ($CuCl_2 \cdot 2H_2O$ and $NiCl_2 \cdot 6H_2O$) undergo electrolysis ($2H_2O + 2e^- \rightarrow H_2 + 2OH^-$), which contributes to the increase in the local pH near the electrode surface, thereby promoting the growth of MOF crystals.[41] In addition, the peak observed at −0.24 V in the first and second cycles might originate from the oxidation of Cu(0), which exists on the electrode surface due to the partial reduction of the Cu^{2+} precursor at the beginning of the growth process.

3.2. Survey of the structure and morphology of the Cu,Ni-BTC film

3.2.1. SEM images and EDX analysis. The morphology of the Cu,Ni-BTC film electrochemically grown on a short GCE *via* a 5-minute synthesis was characterized using the SEM technique. The observed morphology (Fig. 1A) reveals that Cu,Ni-BTC is a porous film that is uniformly distributed on the electrode surface,[42] with a grain size of 50–100 nm. This morphology provides a high surface area, which is very beneficial for improving the sensitivity of the sensor. Fig. 1B displays the EDX spectrum of Cu,Ni-BTC/GCE, which confirms the presence of Cu, Ni, C, and O elements. The elemental composition is given in Table S1. This result shows that in the Cu,Ni-BTC film, the molar ratio of Cu : Ni is 3.67, which is different from the initial precursor ratio of 9 : 1, probably due to the stronger affinity of Ni^{2+} ions for BTC ligands compared to Cu^{2+} ions.

The growth of metal–organic framework (MOF) thin films represents a critical advancement towards integrating MOFs into practical devices such as sensors and optoelectronic devices.[43,44] MOF thin films can be fabricated through various methods, including solvothermal synthesis, layer-by-layer assembly, vapor-phase deposition, and electrochemical techniques.[45,46] Among these, electrodeposition offers distinct benefits, such as mild synthesis conditions at room temperature, short growth times, high scalability, energy efficiency, precise control over the film thickness and homogeneity, and the ability to form uniform coatings on complex geometries without requiring high temperatures or pressures.[47]

3.2.2. XPS analysis. To further confirm the chemical composition and chemical states of the Cu,Ni-BTC film, XPS analysis was used. As shown in the XPS survey spectrum (Fig. 2), the typical peaks for C 1s, O 1s, Cu 2p and Ni 2p are detected, and the elemental composition is shown in Table S2. Noticeably, the molar ratio of Cu : Ni is close to 3.39, aligning with the EDX results discussed above. In the C 1s region, there is one main peak at 284.5 eV (C–C/C=C) and three other peaks at higher binding energies, which correspond to C–O (286.1 eV), O–C=O (288.3 eV) and carbonate (290.7 eV). The O 1s spectrum shows two binding energies corresponding to C=O (531.4 eV) and C–O (533.2 eV). The high-resolution Cu 2p and Ni 2p spectra show the chemical states of Cu^{2+} and Ni^{2+}, respectively.

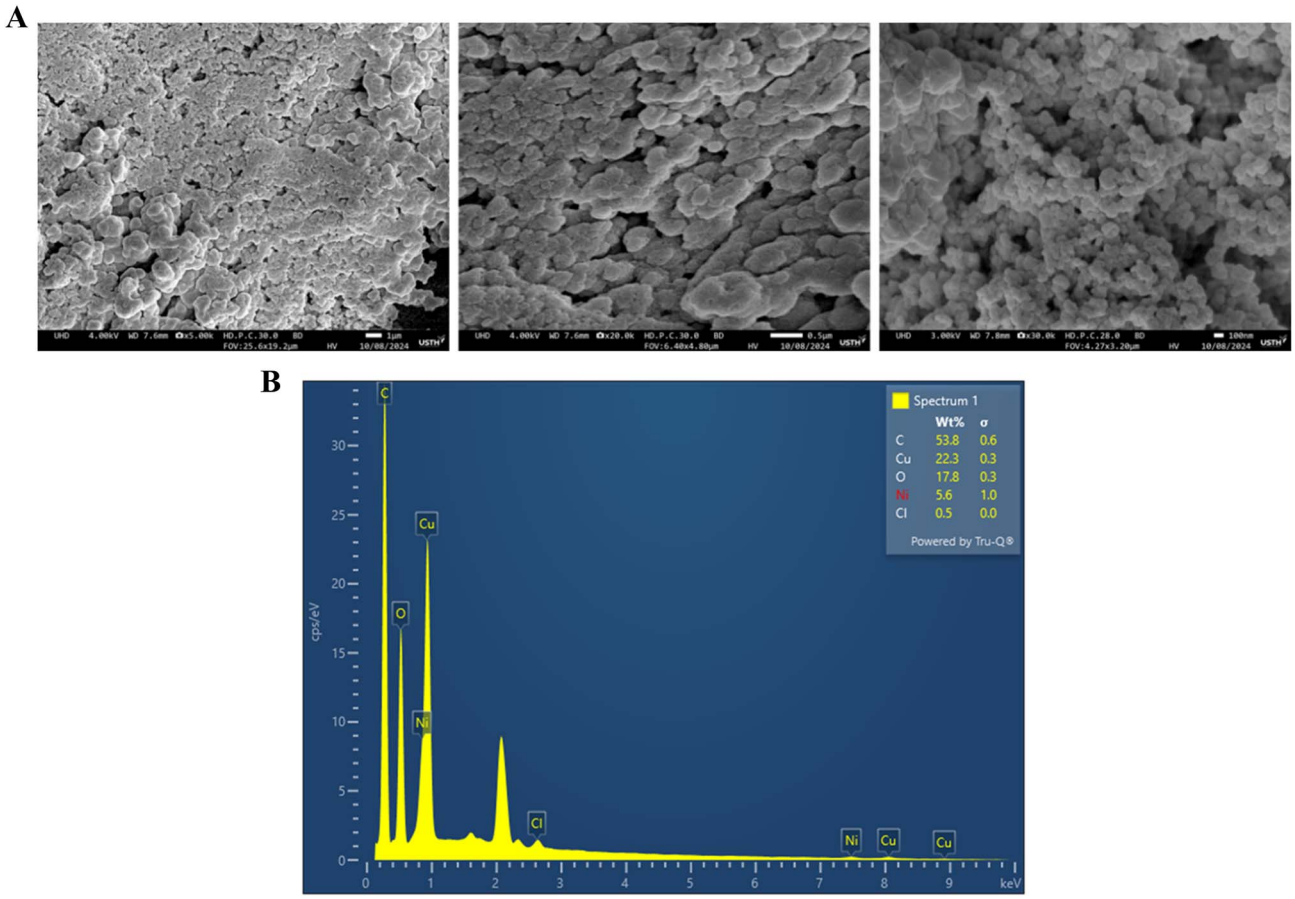

Fig. 1 (A) SEM images and (B) EDX analysis of the electrodeposited Cu,Ni-BTC film.

In the Ni 2p region, the binding energies at 855.7 eV and 861 eV are assigned to Ni $2p_{3/2}$ and its satellite peaks, while the binding energies at 873.5 eV and 878 eV are attributed to Ni $2p_{1/2}$ and its satellite peaks, respectively.[24] In the Cu 2p region, the characteristic Cu^{2+} binding energy peaks are observed at 934.4 eV (Cu $2p_{3/2}$) and 954.3 eV (Cu $2p_{1/2}$), whereas the binding energy peaks located at 932.6 eV (Cu $2p_{3/2}$) and 952.4 (Cu $2p_{1/2}$) are related to Cu^0.[48,49] This indicates that a portion of Cu^{2+} ions in the Cu,Ni-BTC structure is reduced to Cu^0, leading to the coexistence of Cu^{2+} and Cu^0 within the Cu,Ni-BTC structure.

To better understand the state of vacancies in the Cu,Ni-BTC film, we also measured the XPS spectra of Cu-BTC and Ni-BTC films grown *via* a similar approach (see more details in the SI). For the Cu-BTC film, the two peaks associated with Cu^{2+} are observed at 934.7 eV (Cu $2p_{3/2}$) and 954.1 eV (Cu $2p_{1/2}$) in the Cu 2p spectrum, whereas a peak located at 532.0 eV is observed in the O 1s spectrum. For the Ni-BTC film, the two peaks associated with Ni^{2+} are observed at 856.1 eV (Ni $2p_{3/2}$) and 873.7 eV (Ni $2p_{1/2}$) in the Ni 2p spectrum, whereas two peaks located at 531.5 eV and 532.9 eV are observed in the O 1s spectrum. The presence of the satellite peak at a higher binding energy (533.2 eV) in the O 1s spectrum of Cu,Ni-BTC might be due to the increase in the concentration of oxygen vacancies in MOF structures; meanwhile, the shift in the positions of peaks related to Cu^{2+} and Ni^{2+} is ignorable.[50–52]

3.2.3. Raman spectra. Raman spectroscopy is an advanced analytical technique used to identify the bonds present in the Cu,Ni-BTC film, offering profound insights into its framework structures. As seen in Fig. S2, the spectrum reveals typical vibrational modes associated with BTC ligands, such as C–H bonds at 742 cm^{-1} and 827 cm^{-1}, C=C in benzene rings at 1006 cm^{-1}, and the symmetric and asymmetric stretching of O–C–O at 1458 cm^{-1} and 1548 cm^{-1}, respectively.[53] In addition, the vibrational modes relevant to Cu^{2+} ions are observed in the 100–500 cm^{-1} region. Further, the bands at 185 cm^{-1} and 277 cm^{-1} correspond to Cu–O and Cu–Cu atomic vibrations, respectively, while the band at 500 cm^{-1} is linked to Cu–O stretching involving carboxylate bridging oxygen atoms.[53,54] These results indicate the successful coordination of copper ions and nickel ions with BTC.

3.3. Survey of the electrochemical properties of the Cu,Ni-BTC film

3.3.1. Survey with a 0.1 M KCl solution. The electrochemical behavior of the Cu,Ni-BTC film grown at different deposited potentials on the GCE was assessed in a 0.1 M KCl solution. As shown in Fig. 3A, there are two pairs of redox waves in the CV, which are related to the transitions between copper states: Cu(II) + e^- ↔ Cu(I) (111 mV/150 mV) for waves 3/2 and Cu(I) + e^- ↔ Cu (0) (−380 mV/−40 mV) for waves 4/1. In

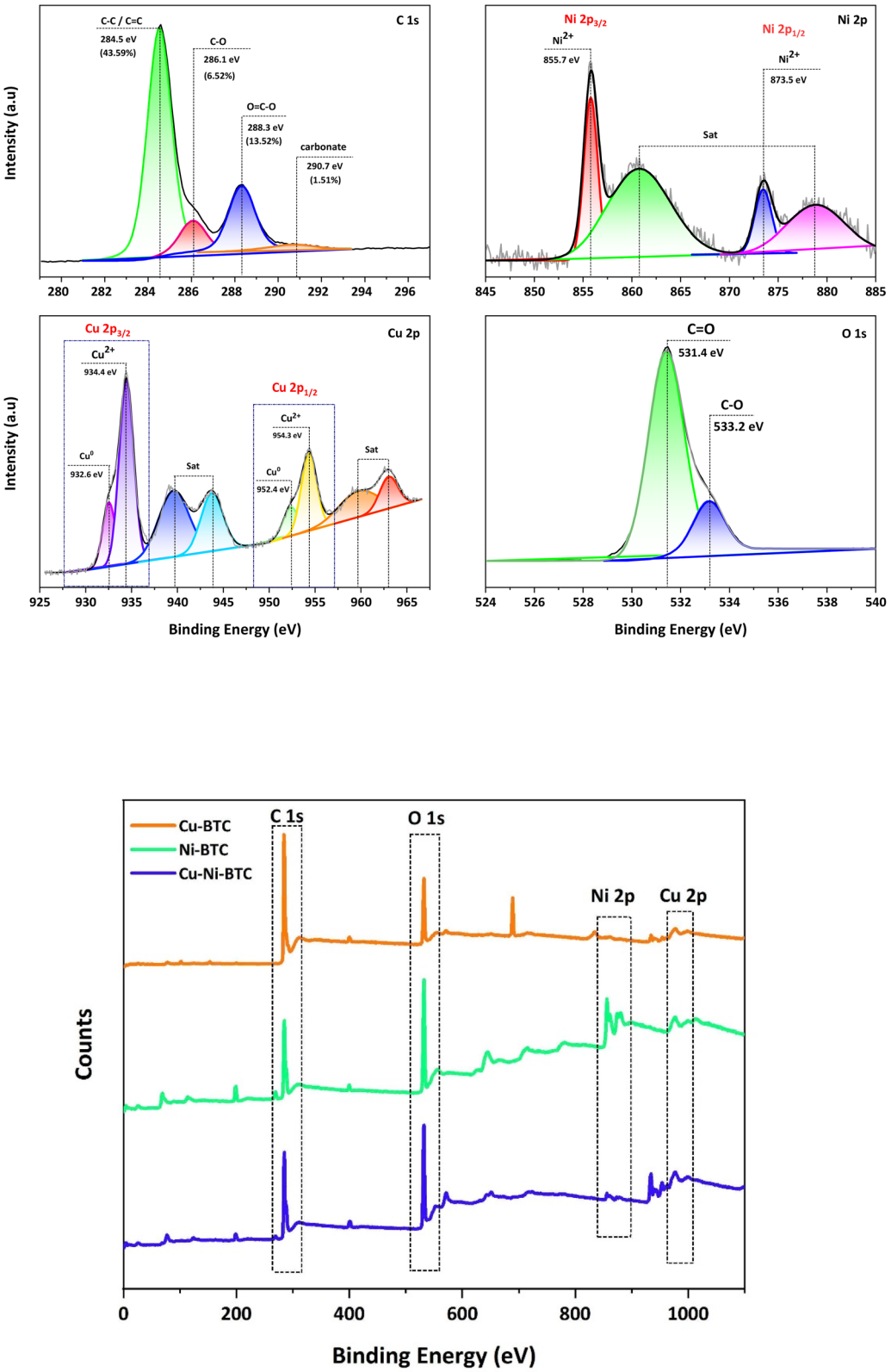

Fig. 2 XPS analysis of the electrodeposited Cu,Ni-BTC film. The survey spectrum and high-resolution C 1s, O 2p, Cu 2p, and Ni 2p spectra were recorded using monochromatic Al–K (1486.6 eV).

addition, a pair of redox waves, 5/6, appears for the Cu,Ni-BTC film deposited at −0.8 V, probably corresponding to the transition of nickel. Furthermore, the magnitude of peak currents varies under different synthesis conditions due to the change in the number of active sites. The highest peak current is recorded for Cu,Ni-BTC deposited at −1 V, with an accumulated charge of

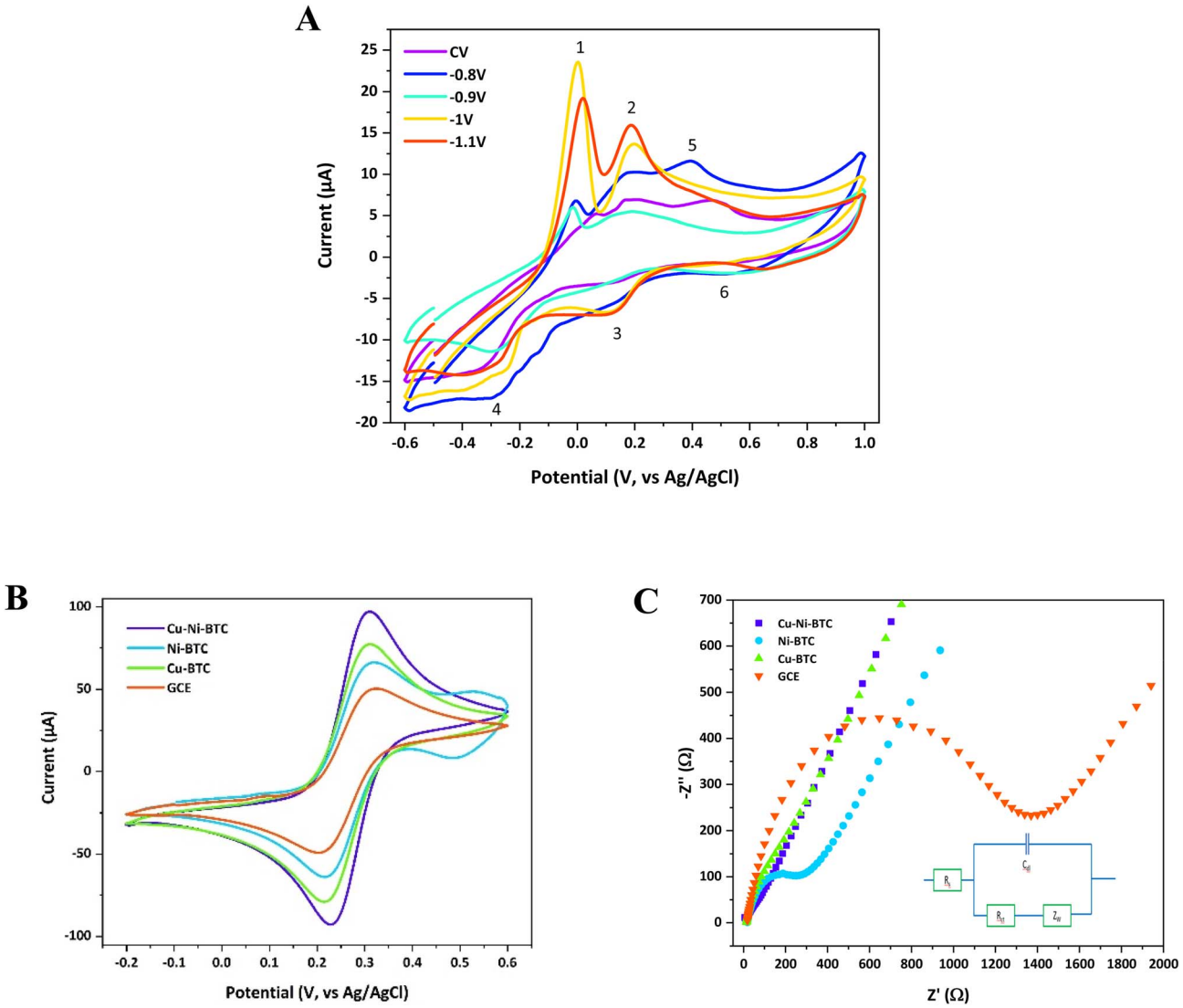

Fig. 3 Analysis of the electrochemical behaviors of the electrodeposited Cu,Ni-BTC film. (A) Cyclic voltammograms recorded in a 100 mM KCl solution. (B) Cyclic voltammograms and (C) EIS spectra recorded in a 100 mM KCl solution containing the 5 mM $[Fe(CN)_6]^{3-/4-}$ probe.

$Q = -11.2$ mC (Table S2). Therefore, this condition was selected for further experiments. It is noteworthy that the charges accumulated at other growth potentials are higher than that at −1 V. By contrast, the amount of the MOF material deposited on the electrode surface at −1 V might not be as much as that at other potentials. Nevertheless, the slow growth speed of the MOF film with a suitable thickness and good uniformity might lead to better charge transfer kinetics at the electrode/electrolyte interface.

3.3.2. Survey with a 0.1 M KCl solution containing $[Fe(CN)_6]^{3-/4-}$. The electron transfer properties of the bare GCE, Cu-BTC/GCE, Ni-BTC/GCE, and Cu,Ni-BTC/GCE were also investigated by EIS and CV in a 0.1 M KCl electrolyte solution containing 5 mM $[Fe(CN)_6]^{3-/4-}$ as a redox probe. Fig. 3B shows the reversible redox reaction of $Fe^{2+/3+}$ on the surface of the GCE and GCE modified with MOF materials. Compared to the bare GCE, the peak currents increase by 49%, while the peak separation drops by 25 mV on the electrode modified with the grown Cu,Ni-BTC film. These findings are consistent with the results from EIS spectra (Fig. 3C), where the charge transfer resistance of Cu,Ni-BTC/GCE (58.7 Ω) is much smaller than that of the bare GCE (1286 Ω) (Table S3). The charge transfer kinetics at the electrode/electrolyte interface on the electrode modified with the bimetallic MOF (Cu,Ni-BTC) are also found be better than that on the electrode modified with homometallic MOF materials (Cu-BTC and Ni-BTC).[44,55] These results suggest that there is a synergistic effect in the bimetallic MOF, Cu,Ni-BTC, which enhances the electron transfer.[23]

3.4. Mechanism of the oxidation of caffeic acid on the Cu,Ni-BTC film

3.4.1. Cyclic voltammograms. The oxidation of CA (100 μM) on the surface of electrodes was tested by CV. The MOF films (Ni-BTC, Cu-BTC, and Cu,Ni-BTC) were synthesized on GCEs by

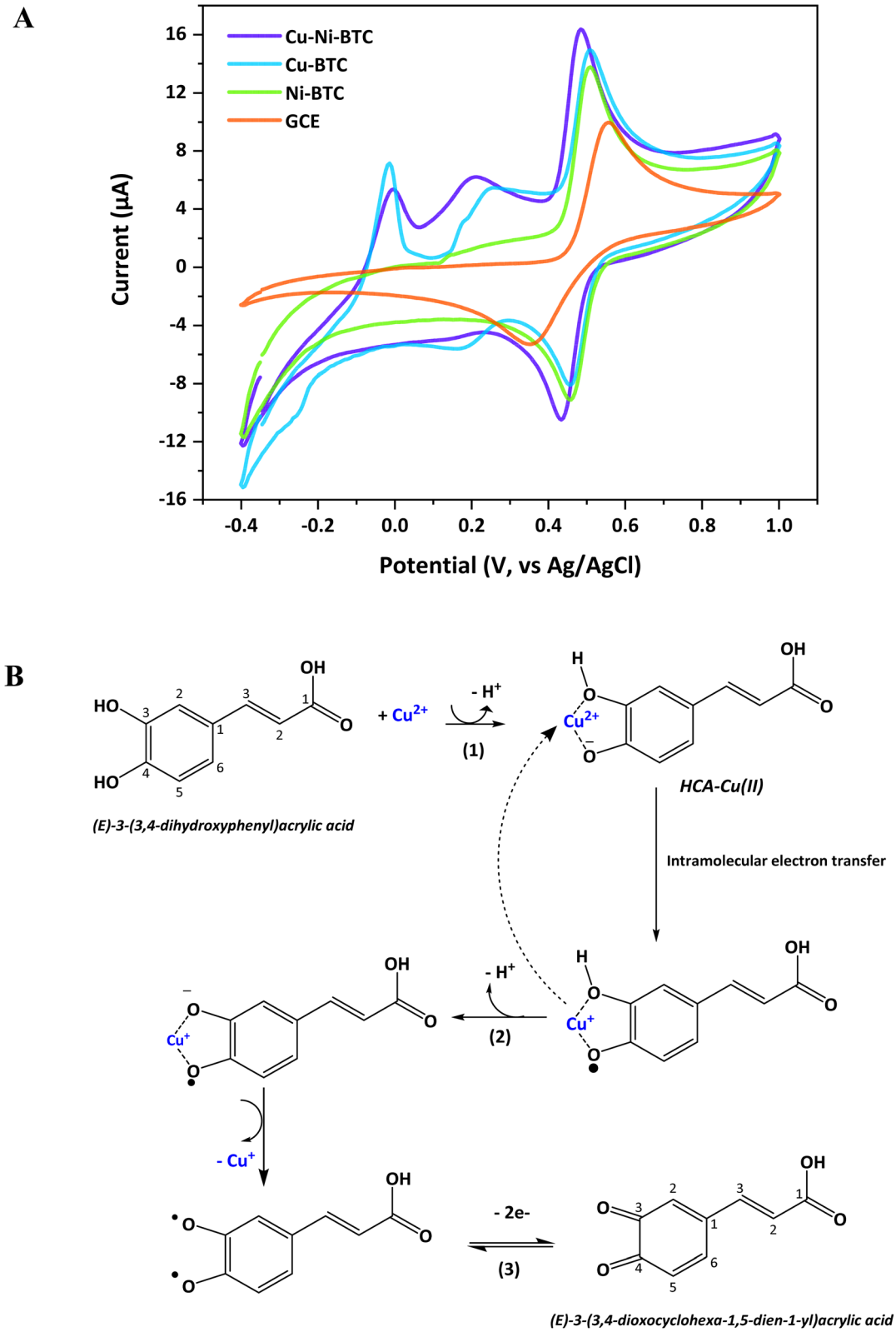

Fig. 4 Mechanism for the electrochemical oxidation and reduction of caffeic acid on the electrodeposited Cu,Ni-BTC film. (A) Cyclic voltammograms recorded on the Cu,Ni-BTC film, Cu-BTC, Ni-BTC and GCE in a PBS solution (pH 3) containing 500 μM caffeic acid and (B) the proposed redox mechanism of CA on the Cu,Ni-BTC film.[52]

chronoamperometry at −1 V for 5 minutes. The effects of the scan rate and pH were also investigated to better understand the redox mechanism of CA on the surface of the GCE and modified GCEs.

CV was employed to investigate the electrochemical behavior of CA on the bare GCE, Ni-BTC/GCE, Cu-BTC/GCE, and Cu,Ni-BTC/GCE in the presence of 500 μM CA in a PBS buffer with pH = 3 at a scan rate of 50 mV s^{-1} (Fig. 4). It can be seen that the peak separation was shortened (by 160 mV) and the peak current was increased (by 1.5 times) on the Cu,Ni-BTC-modified GCE compared with the bare electrode. As mentioned above, the good electrocatalytic activity of bimetallic centers and the effective adsorption of target molecules inside the porous structure of the Cu,Ni-BTC film are mainly responsible for such good kinetics of electrochemical reactions.

3.4.2. Proposed mechanism. The mechanism of CA oxidation on the Cu,Ni-BTC film is proposed in Fig. 4B. The metal centers (M) in the MOF structure actively participate in the oxidation of CA as follows: (1) the catechol groups (two adjacent –OH groups) chelate with M(II) to form the HCA-M(II) complex; (2) the HCA-M(II) complex undergoes intramolecular electron transfer to form Cu(I) and an *ortho*-semiquinone radical anion; and (3) the *ortho*-semiquinone radical anion can be easily oxidized to release two electrons and provide the final product *ortho*-quinone. The oxidation and reduction peaks are observed at 0.49 V and 0.44 V, respectively, corresponding to the formation and decomposition of *ortho*-quinone.[17,56] It has been previously reported that CuO nanoparticles and Cu^{2+}-doped systems might help enhance the electrochemical oxidation of caffeic acid by facilitating charge transfer,[17,18] whereas Ni^{2+} often shows catalytic activity in the oxidation of organic compounds in enzymatic or biomimetic systems.[57–60] Bimetallic Cu–Ni systems have also shown promise in the electrochemical oxidation of other phenolic compounds.[61]

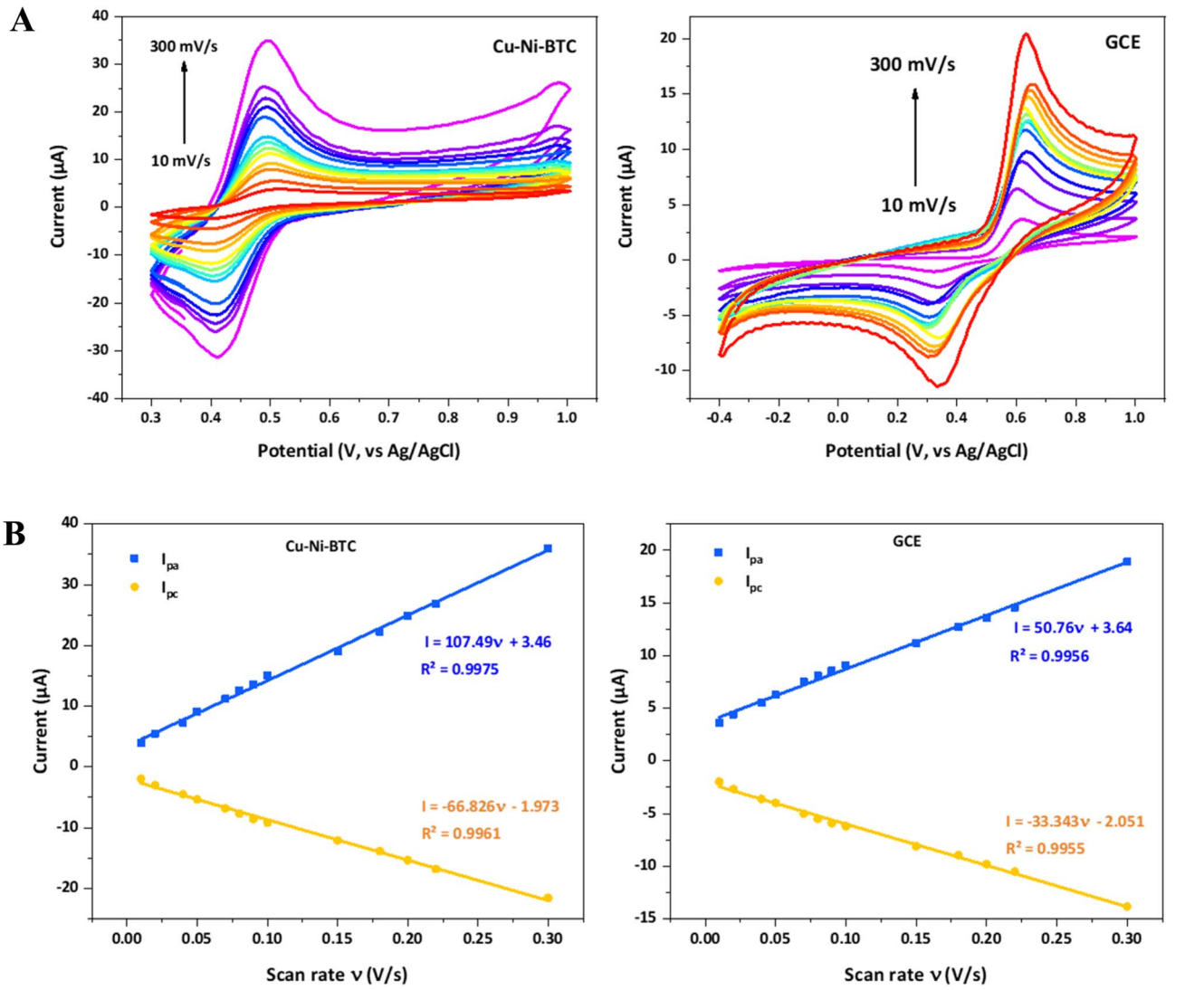

Fig. 5 Effect of the scan rate on the redox behaviors of caffeic acid on the electrodeposited Cu,Ni-BTC film. (A) Cyclic voltammograms recorded on the electrodeposited Cu,Ni-BTC film and bare GCE in a PBS solution (pH 3) containing 500 μM caffeic acid at different scan rates. (B) The anodic and cathodic currents as a function of the scan rate in the linear form.

The oxidation of CA on the bare GCE follows a different reaction pathway (Fig. S3). At anodic potentials, one hydroxyl group (–OH) on the catechol loses an electron (−e) to the electrode, generating a semiquinone radical (–O$^{\bullet}$) on the aromatic ring. Simultaneously, one proton (H^+) from the –OH group is released into the solution, and the resonance is stabilized across the aromatic ring. Then, the second hydroxyl group loses another electron and proton to form *ortho*-quinone.[62] Because the *ortho*-quinone has a conjugated system with double bonds and a carbonyl group (C=O), it can more easily receive $2e^-$ and $2H^+$ to regenerate CA.

The key difference in the oxidation mechanisms of CA on the bare and modified electrodes is related to the presence of metal centers. In the case of the bare electrode, the electrochemical oxidation of CA is simply governed by the charge exchange between the electrode surface and CA molecules; thus, the recorded signals are not very high, and the oxidation process is more reversible. Otherwise, there is a strong involvement of metal ions in the electrochemical oxidation of CA molecules on MOF-modified electrodes; then, the electrochemical signals are much improved, whereas the reaction is somehow quasi-reversible (as discussed in the next sections).

3.4.3. Effect of the scan rate. The effect of the scan rate on the redox behavior of CA was studied at scan rates ranging from 10 to 300 mV s^{-1}. As shown in Fig. 5, the cathodic/anodic peak current intensity increases linearly with the scan rate for both bare and modified GCEs, which indicates an adsorption-controlled kinetics process. Noticeably, the slopes of (I_{pa}–ν) and (I_{pc}–ν) curves of Cu,Ni-BTC/GCE are twice as high as those of the bare GCE. This result further confirms the improved kinetics of the redox reactions of CA on the electrochemically grown Cu,Ni-BTC film.

3.4.4. Effect of pH. Caffeic acid can exist in several ionic forms, depending on the pH, because its structure contains one carboxyl group and two phenolic hydroxyl groups (Fig. S4). Therefore, the medium's pH value significantly influences the electrochemical behavior of CA, resulting in distinct CV responses across the pH range from 3 to 8 (Fig. 6). As seen in Fig. 6, the position of the oxidation peak was negatively shifted as follows: $E_{pa}(V) = -0.041\ pH + 0.608$ ($R^2 = 0.9869$) and $E_{pc}(V) = -0.056\ pH + 0.593$ ($R^2 = 0.971$) for Cu,Ni-BTC/GCE; $E_{pa}(V) = -0.0198\ pH + 0.6101$ ($R^2 = 0.9854$) and $E_{pc}(V) = -0.071\ pH + 0.543$ ($R^2 = 0.973$) for the bare GCE. The slopes of (E_{pa}–pH) and (E_{pc}–pH) curves for the Cu,Ni-BTC-modified GCE were determined to be 41 mV pH^{-1} and 56 mV pH^{-1}, respectively. This value is close to the theoretical Nernstian value (59 mV pH^{-1}), indicating the participation of an equal number of protons and electrons in the oxidation process. These findings are consistent with the report of Hotta *et al.*, who suggested that the number of electrons involved in the oxidation reaction of CA is equal to 2 at pH values lower than 7,[63] and in agreement with the proposed reaction mechanism (Fig. 4B), in which two electrons and two protons are involved in the reaction. Otherwise, the slopes of (E_{pa}–pH) and (E_{pc}–pH) curves were 19.8 mV pH^{-1} and 71 mV pH^{-1}, respectively, for the oxidation of CA on the bare GCE. Moreover, an increase in the pH (3.0–8.0) resulted in a decrease in the current intensity, and the highest current response was recorded at pH 3.0. It has been previously reported that a change in the ionic species of CA in the solution (Fig. S4) might lead to a smaller number of protons participating in the reaction at pH > 7.[62]

3.5. Sensing performances

3.5.1. Calibration curves. DPV is a preferred technique because it provides a clearer signal and higher sensitivity, minimizes the background current, and shortens the measurement time compared to CV. It was found that the oxidation peaks of CA in DPV curves (Fig. 7A) were shifted to lower potentials on the Cu,Ni-BTC film (450 mV) compared to those on the bare electrode (550 mV). This result provides one more piece of evidence for the electrocatalytic activity of the bimetallic MOF film towards the electrochemical oxidation of CA. The calibration curves were extracted from DPV curves recorded on bare and modified electrodes at CA concentrations in the range of 0–25 μM at an optimal pH (pH = 3) (Fig. 7B). The linear regression equations are expressed as follows: $I\ (\mu A) = 0.0647 \times C_{\text{caffeic acid}}\ (\mu M) - 0.0485$ ($R^2 = 0.9987$) for Cu,Ni-BTC/GCE; $I\ (\mu A) = 0.0049 \times C_{\text{caffeic acid}}\ (\mu M) + 0.004$ ($R^2 = 0.997$) for GCE (Table 1). The limit of detection (LOD) was calculated from the standard deviation (SD) of the intercept and the slope (b) of regression equations: LOD = 3 × SD/b, whereas the sensitivity of the sensor (S) is the slope of the calibration curve. The sensitivity and LOD of the as-prepared CA sensor based on the electrochemically grown Cu,Ni-BTC film were 0.924 μA μM^{-1} cm^{-2} and 0.7 μM, respectively. This means that the Cu,Ni-BTC film helps improve the sensitivity and LOD of the CA sensor by 13.2 and 1.5 times compared to the unmodified electrode, respectively (Table 1). Compared to previously reported studies, our sensor exhibits good sensing performance with a lower LOD and a wide linear range, as presented in Table 2.

3.5.2. Reproducibility and stability tests. The reproducibility of the sensor was determined by analyzing the DPV signals of seven identically fabricated Cu,Ni-BTC/GCEs under the same conditions in a 20 μM CA solution (Fig. 8A). A relative standard deviation (RSD) of 2.61% was obtained (Table S4), indicating the high reproducibility of the as-fabricated CA sensor.

The stability study was carried out by synthesizing a Cu,Ni-BTC-modified GCE and performing daily DPV measurements in a PBS solution (pH = 3) containing 20 μM CA for seven consecutive days (Fig. 8B). It was found that the as-prepared sensor exhibited good stability for one week with RSD = 6.47% (Table S5) and then started to decay, and the RSD remained only 11.37% on the 11th day.

3.5.3. Interference study. To evaluate the selectivity of Cu,Ni-BTC/GCE for CA detection, an interference study was performed by introducing various potential interfering compounds (500 μM each) such as GA, AA, and UA at a fixed CA concentration of 500 μM. The bar chart in Fig. 8C illustrates the impact of these interference molecules on the redox behavior of CA. The addition of AA and UA slightly altered the peak oxidation current intensity (less than 5%) of CA in the DPV response. However, GA caused a more noticeable impact, reducing the

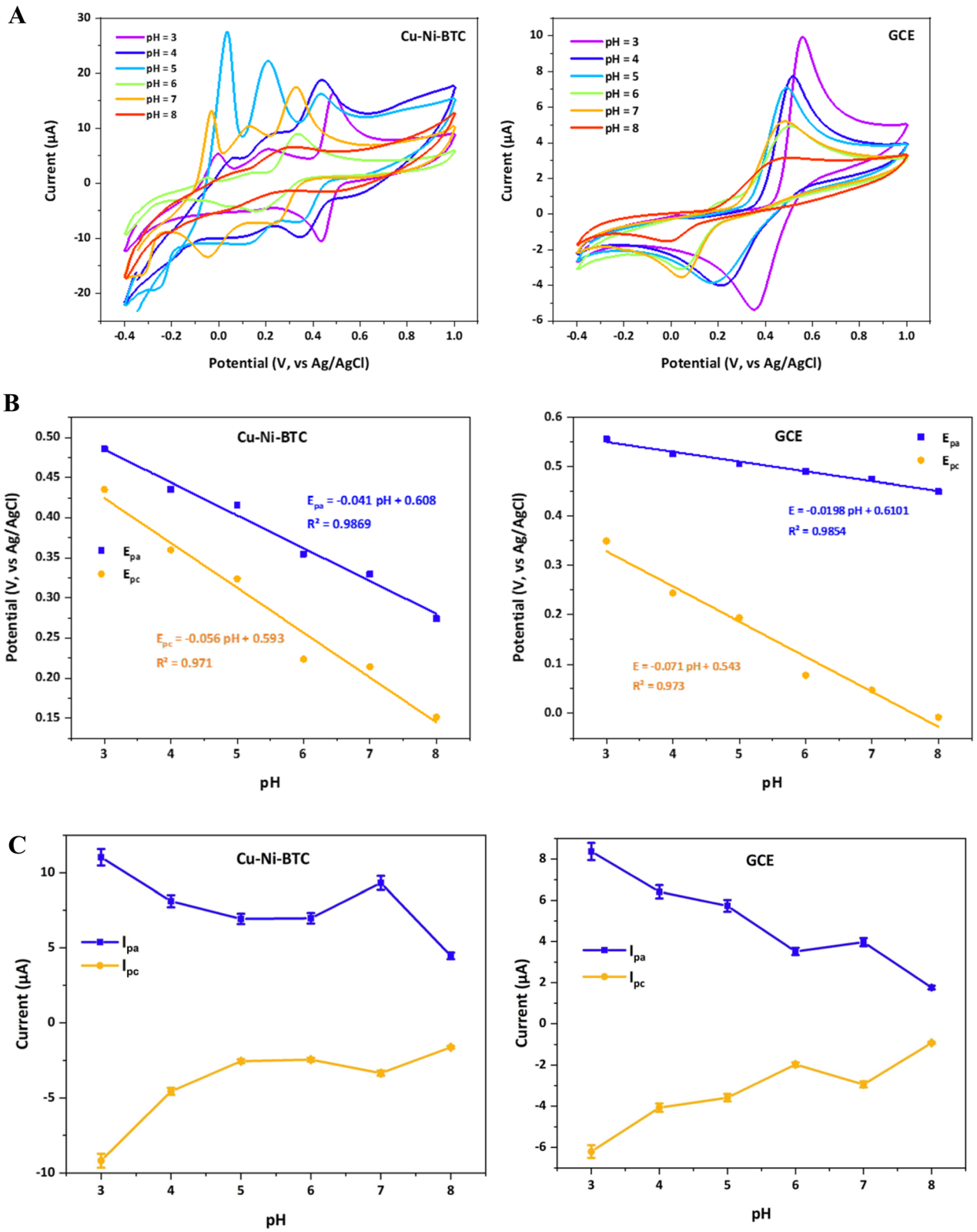

Fig. 6 Effect of the pH on the redox behaviors of caffeic acid on the electrodeposited Cu,Ni-BTC film. (A) Cyclic voltammograms recorded on the electrodeposited Cu,Ni-BTC film and bare GCE at different pH (3–8). (B) The shift in redox potentials and (C) the variation in redox currents with increasing pH; values represent mean ± SD (n = 3).

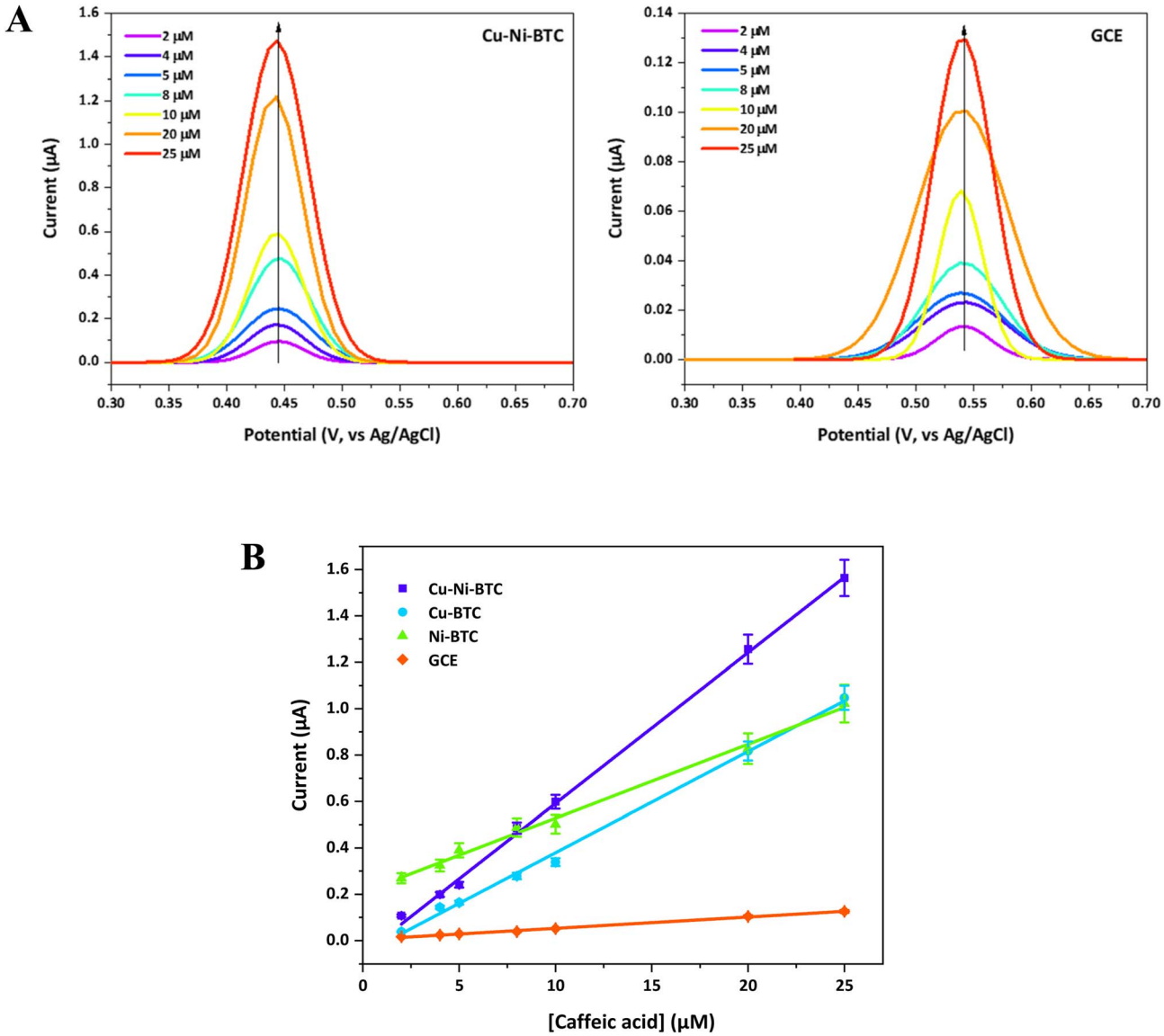

Fig. 7 Detection of caffeic acid using the electrodeposited Cu,Ni-BTC film. (A) DPV curves recorded on the electrodeposited Cu,Ni-BTC film and bare GCE in PBS (pH 3) containing caffeic acid at different concentrations (2–25 μM). (B) Calibration curves; values represent mean ± SD ($n = 3$).

Table 1 Comparison of sensing performances towards the electrochemical detection of caffeic acid for electrodes modified with electrodeposited MOF films in this work

Electrode	Linear range (μM)	Regression equation	Sensitivity (μA μM^{-1} cm^{-2})	LOD (μM)	LOQ (μM)
Cu,Ni-BTC	2–25	I (μA) = 0.0647 × $C_{\text{caffeic acid}}$ (μM) − 0.0485 (R^2 = 0.9987)	0.924	0.70	2.33
Cu-BTC	2–25	I (μA) = 0.0437 × $C_{\text{caffeic acid}}$ (μM) − 0.0576 (R^2 = 0.9968)	0.624	1.11	3.70
Ni-BTC	2–25	I (μA) = 0.0319 × $C_{\text{caffeic acid}}$ (μM) + 0.2092 (R^2 = 0.9946)	0.456	1.44	4.80
Bare GCE	2–25	I (μA) = 0.0049 × $C_{\text{caffeic acid}}$ (μM) + 0.0040 (R^2 = 0.997)	0.070	1.07	3.57

peak current of CA by 14.3%, which is likely because its redox potential is very close to that of CA (500 mV *vs.* 450 mV). These results indicate the acceptable selectivity of the electrochemical sensor based on the electrochemically grown Cu,Ni-BTC film for the electrochemical detection of CA.

3.5.4. Real sample study. A real sample study was conducted to detect CA in apple juice using the spiked-recovery

Table 2 Comparison of sensing performances towards the electrochemical detection of caffeic acid for the sensors prepared in this work and in previous works[a]

Electrode	Matrix/sample	Linear range (μM)	Sensitivity (μA μM^{-1} cm^{-2})	LOD (μM)	References
CuO/GCE	Caffeinated drinks	0.05–229.5	0.0722	0.04	18
GR/CuO@Cu-BTC/GCE	Red wine	0.02–10	1.873	0.007	28
CuONPs/CPE	Honey	5.0–50.0	0.9677	3.21	17
DL-PAMMCNTPE	Apple juice and coffee powder	20–600	—	0.28	64
Co-NC/MWCNTs/GCE	Food samples	0.5–50	—	0.162	65
CaO/g-C_3N_4/PVA/GCE	Blood plasma samples	0.01–70	—	0.0024	66
PtNi/C/GCE	Wine samples	0.75–591.783	0.0389	0.5	16
		111.783–591.783	0.0107		
$CoFeSe_2$/f-CNF/GCE	Wine sample	0.01–263.96	2.04	0.002	67
MCO/GR/GCE	Food sample	0.01–0.69	1.494	0.003	68
Cu,Ni-BTC/GCE	Apple juice	2–25	0.924	0.7	This work

[a] Note: DL-PAMMCNTPE, DL-phenylalanine (DL-PA)-modified multiwalled carbon nanotube paste electrode.

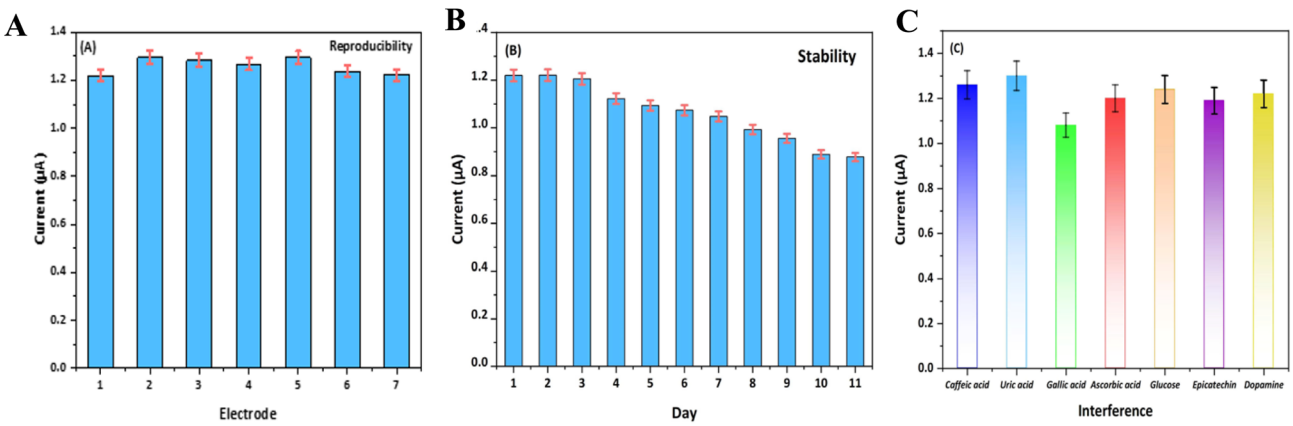

Fig. 8 (A) Reproducibility, (B) stability and (C) interference tests. Values represent mean ± SD ($n = 3$).

method. The sample preparation procedure is detailed in the Experiment Section. The DPV curves were recorded when Cu,Ni-BTC/GCE was immersed in the as-prepared sample solution. The DPV curves and calibration curves of the standard addition method were previously recorded and are given in Fig. S5. The concentration of CA in the real sample was calculated to be 28.09 μM. The recovery percentages for CA ranged from 92.2% to 98.4% (Table S7). These results demonstrate the possibility of using the Cu,Ni-BTC/GCE sensor in practical applications for assessing the quality of fruits, foods, and other stuffs containing a considerable amount of caffeic acid.

4. Conclusions

In this study, we successfully developed an electrochemical sensor for *in situ* CA determination using an electrochemically grown bimetallic MOF film (Cu,Ni-BTC). The results demonstrated that the Cu,Ni-BTC-modified electrode had higher conductivity and electron transfer ability than the homometallic Cu-BTC, Ni-BTC and bare electrode. The sensitivity and LOD of the as-prepared Cu,Ni-BTC/GCE for CA detection were 0.924 μA μM^{-1} cm^{-2} (improved by 13.2 times compared to the bare electrode) and 0.7 μM (improved by 1.5 times compared to the bare electrode), respectively. The developed sensor also exhibited high reproducibility (RSD = 2.61%), good stability (RSD = 6.47%), and good recovery in real samples (92.5–95%). These findings pave the way to developing highly uniform porous films based on metal–organic framework structures for further sensing applications. In the near future, our research team will focus more on the formation of uniform and thin MOF films that exhibit many interesting electronic behaviors (*i.e.*, gating effect in transistors) for other sensing applications.

Conflicts of interest

There are no conflicts to declare.

Data availability

The data supporting this article have been included as part of the supplementary information (SI). Supplementary information is available. See DOI: https://doi.org/10.1039/d5ra08073h.

Acknowledgements

The authors would like to express our sincere thanks to the financial support from University of Science and Technology of Hanoi (USTH) for research group "Sensing systems based on Electronic NanoStructures (SENS)" (SENS) through the research program for promoting emerging and top-tier research groups at USTH.

References

1 A. Birková, Caffeic acid: a brief overview of its presence, metabolism, and bioactivity, *Bioact. Compd. Health Dis.*, 2020, **3**, 74.
2 K. M. M. Espíndola, *et al.*, Chemical and Pharmacological Aspects of Caffeic Acid and Its Activity in Hepatocarcinoma, *Front. Oncol.*, 2019, **9**, 541.
3 K. Celińska-Janowicz, *et al.*, Constituents of Propolis: Chrysin, Caffeic Acid, p-Coumaric Acid, and Ferulic Acid Induce PRODH/POX-Dependent Apoptosis in Human Tongue Squamous Cell Carcinoma Cell (CAL-27), *Front. Pharmacol*, 2018, **9**, 336.
4 E. Pinho, *et al.*, Antibacterial Potential of Northeastern Portugal Wild Plant Extracts and Respective Phenolic Compounds, *BioMed Res. Int.*, 2014, **2014**, 1–8.
5 H. Utsunomiya, *et al.*, Inhibition by caffeic acid of the influenza A virus multiplication in vitro, *Int. J. Mol. Med.*, 2014, **34**, 1020–1024.
6 D. Huang, *et al.*, Evaluation on monoamine neurotransmitters changes in depression rats given with sertraline, meloxicam or/and caffeic acid, *Genes Dis.*, 2019, **6**, 167–175.
7 M. Yazar, M. Sevindik, I. Uysal and A. O. Polat, Effects of Caffeic Acid on Human Health: Pharmacological and Therapeutic Effects, Biological Activity and Toxicity, *Pharm. Chem. J.*, 2025, **59**, 49–55.
8 H. Wang, Determination of rosmarinic acid and caffeic acid in aromatic herbs by HPLC, *Food Chem.*, 2004, **87**, 307–311.
9 O. J. Lara-Guzmán, R. Álvarez-Quintero, E. Osorio, M. Naranjo-Cano and K. Muñoz-Durango, GC/MS method to quantify bioavailable phenolic compounds and antioxidant capacity determination of plasma after acute coffee consumption in human volunteers, *Food Res. Int.*, 2016, **89**, 219–226.
10 N. Z. Alzoman, *et al.*, CE-DAD Determination of Scutellarein and Caffeic Acid in Abelia triflora Crude Extract, *J. Chromatogr. Sci.*, 2018, **56**, 746–752.
11 V. Karabozhikova and V. Tsakova, Electroanalytical determination of caffeic acid – Factors controlling the oxidation reaction in the case of PEDOT-modified electrodes, *Electrochim. Acta*, 2019, **293**, 439–446.
12 L. C. Almeida, *et al.*, Electrochemical deposition of bio-inspired laccase-polydopamine films for phenolic sensors, *Electrochim. Acta*, 2019, **319**, 462–471.
13 D. E. F. dos Santos, *et al.*, A Sustainable Nanomaterial Based on Gold Nanoparticles and Graphene for Highly Sensitive Electrochemical Sensing of Caffeic Acid in Coffees, *Food Anal. Methods*, 2024, **17**, 1348–1358.
14 G. Kesavan, T. Subramaniam and H. V. Manemaran, Development of Promising Flower-like Ag/$SrFeO_3$ Nanosheet Electrode Materials: An Efficient and Selective Electrocatalytic Detection of Caffeic Acid in Coffee and Green Tea, *ACS Omega*, 2023, **8**, 46414–46424.
15 Y. Li, *et al.*, An ultrasensitive dietary caffeic acid electrochemical sensor based on Pd-Ru bimetal catalyst doped nano sponge-like carbon, *Food Chem.*, 2023, **425**, 136484.
16 J. Wang, *et al.*, Ultra-stable Electrochemical Sensor for Detection of Caffeic Acid Based on Platinum and Nickel Jagged-Like Nanowires, *Nanoscale Res. Lett.*, 2019, **14**, 11.
17 M. G. Galugerdi, E. Mahmoodi-Khaledi and H.-A. Rafiee-Pour, Detection of caffeic acid in honey using carbon paste electrode modified by copper (II) oxide (CuO) nanoparticles, *Sci. Rep.*, 2025, **15**, 23397.
18 A. Venkadesh, J. Mathiyarasu and S. Radhakrishnan, MOF mediated synthesis of porous copper oxide and their electrochemical sensing of caffeic acid in caffeinated drinks, *Inorg. Chem. Commun.*, 2021, **128**, 108573.
19 B. Parasuraman, *et al.*, Rapid detection of caffeic acid in food beverages using a non-enzymatic electrochemical sensor based on a Bi_2S_3/CNF nanocomposite, *Sustainable Food Technol.*, 2024, **2**, 717–728.
20 Y. A. Kumar, *et al.*, A review on in-plane ordered MXenes-based materials in addressing challenges faced by biosensor applications, *J. Energy Storage*, 2025, **121**, 116507.
21 Y. Xu, Q. Li, H. Xue and H. Pang, Metal-organic frameworks for direct electrochemical applications, *Coord. Chem. Rev.*, 2018, **376**, 292–318.
22 H. Furukawa, K. E. Cordova, M. O'Keeffe and O. M. Yaghi, The Chemistry and Applications of Metal-Organic Frameworks, *Science*, 2013, **341**, 1230444.
23 L. Chen, H.-F. Wang, C. Li and Q. Xu, Bimetallic metal–organic frameworks and their derivatives, *Chem. Sci.*, 2020, **11**, 5369–5403.
24 J. Wan, *et al.*, Transition Bimetal Based MOF Nanosheets for Robust Aqueous Zn Battery, *Front. Mater.*, 2020, **7**, 194.
25 X. Gong, *et al.*, A highly sensitive sensing strategy based on 2D bimetallic MOFs and multi-walled carbon nanotubes, *Microchem. J.*, 2024, **205**, 111135.
26 N. N. Tien, *et al.*, Cu,Zr-BTC/CNT composite for electrochemical detection of endocrine disruptor bisphenol A, *J. Mater. Sci.*, 2023, **58**, 16699–16713.
27 X. Huang, *et al.*, Fabrication of novel electrochemical sensor based on bimetallic Ce-Ni-MOF for sensitive detection of bisphenol A, *Anal. Bioanal. Chem.*, 2020, **412**, 849–860.
28 X. Tu, *et al.*, Self-template synthesis of flower-like hierarchical graphene/copper oxide@copper(II) metal-organic framework composite for the voltammetric determination of caffeic acid, *Microchim. Acta*, 2020, **187**, 258.
29 L. Zheng, *et al.*, In Situ NH_2-MIL-101(Fe) Nanoparticles Modified Pencil Core Electrodes for Simultaneous Ratiometric Electrochemical Detection of Caffeic Acid and

Acetaminophen, *ACS Appl. Nano Mater.*, 2024, **7**, 16295–16305.
30 I. Stassen, *et al.*, Chemical vapour deposition of zeolitic imidazolate framework thin films, *Nat. Mater.*, 2016, **15**, 304–310.
31 O. Shekhah, *et al.*, Controlling interpenetration in metal–organic frameworks by liquid-phase epitaxy, *Nat. Mater.*, 2009, **8**, 481–484.
32 K. B. Lausund and O. Nilsen, All-gas-phase synthesis of UiO-66 through modulated atomic layer deposition, *Nat. Commun.*, 2016, **7**, 13578.
33 X. Zhang, *et al.*, Electrochemical deposition of metal–organic framework films and their applications, *J. Mater. Chem. A*, 2020, **8**, 7569–7587.
34 M. S. Hosseini, S. Zeinali and M. H. Sheikhi, Fabrication of capacitive sensor based on Cu-BTC (MOF-199) nanoporous film for detection of ethanol and methanol vapors, *Sens. Actuators, B*, 2016, **230**, 9–16.
35 J. Feng, T.-F. Liu and R. Cao, An Electrochromic Hydrogen-Bonded Organic Framework Film, *Angew. Chem., Int. Ed.*, 2020, **59**, 22392–22396.
36 J. Huang, *et al.*, Electrochemical Exfoliation of Pillared-Layer Metal–Organic Framework to Boost the Oxygen Evolution Reaction, *Angew. Chem., Int. Ed.*, 2018, **57**, 4632–4636.
37 B. Zhang, *et al.*, One-step controlled electrodeposition of iron-based binary metal organic nanocomposite, *Appl. Surf. Sci.*, 2020, **504**, 144504.
38 M. Li and M. Dincă, Selective formation of biphasic thin films of metal–organic frameworks by potential-controlled cathodic electrodeposition, *Chem. Sci.*, 2014, **5**, 107–111.
39 M. Li and M. Dincă, On the Mechanism of MOF-5 Formation under Cathodic Bias, *Chem. Mater.*, 2015, **27**, 3203–3206.
40 V. Rosca, M. Duca, M. T. de Groot and M. T. M. Koper, Nitrogen Cycle Electrocatalysis, *Chem. Rev.*, 2009, **109**, 2209–2244.
41 N. Campagnol, *et al.*, On the electrochemical deposition of metal–organic frameworks, *J. Mater. Chem. A*, 2016, **4**, 3914–3925.
42 N. Tien Dat, N. Ngoc Tien, N. T. T. Ngan and V. Thi Thu, Sensing interface based on electrodeposited Cu-BTC microporous film for electrochemical detection of the painkiller paracetamol, *Analyst*, 2023, **148**, 1777–1785.
43 M. M. Sabzehmeidani and M. Kazemzad, Recent advances in surface-mounted metal–organic framework thin film coatings for biomaterials and medical applications: a review, *Biomater. Res.*, 2023, **27**, 115.
44 M. M. Sabzehmeidani, S. Gafari, S. jamali and M. Kazemzad, Concepts, fabrication and applications of MOF thin films in optoelectronics: A review, *Appl. Mater. Today*, 2024, **38**, 102153.
45 L. Xue, G. Luo, X. Yang, Y. Qin and B. Zhang, Vapor-phase methods for synthesizing metal-organic framework thin films, *Innovation Mater.*, 2024, **2**, 100047.
46 A. Bétard and R. A. Fischer, Metal–Organic Framework Thin Films: From Fundamentals to Applications, *Chem. Rev.*, 2012, **112**, 1055–1083.
47 W.-J. Li, M. Tu, R. Cao and R. A. Fischer, Metal–organic framework thin films: electrochemical fabrication techniques and corresponding applications & perspectives, *J. Mater. Chem. A*, 2016, **4**, 12356–12369.
48 J. Zhang, T. Zhou and L. Wen, Selective Metallization Induced by Laser Activation: Fabricating Metallized Patterns on Polymer via Metal Oxide Composite, *ACS Appl. Mater. Interfaces*, 2017, **9**, 8996–9005.
49 Y. Shao, *et al.*, Degradation of chlortetracycline with simultaneous removal of copper (II) from aqueous solution using wheat straw-supported nanoscale zero-valent iron, *Chem. Eng. J.*, 2020, **379**, 122384.
50 L. Zhang, H. Yu, L. Han and K. Tao, Vacancy engineering of metal–organic framework derivatives for supercapacitors and electrochemical water splitting, *Chem. Commun.*, 2025, **61**, 8830–8842.
51 C. Chen, X. Ji, Y. Xiong and J. Jiang, Ni/Ce co-doping metal–organic framework catalysts with oxygen vacancy for catalytic transfer hydrodeoxygenation of lignin derivatives vanillin, *Chem. Eng. J.*, 2024, **481**, 148555.
52 G. S. More, A. K. Kar and R. Srivastava, Cu–Ce Bimetallic Metal–Organic Framework-Derived, Oxygen Vacancy-Boosted Visible Light-Active Cu2O–CeO2/C Heterojunction: An Efficient Photocatalyst for the Sonogashira Coupling Reaction, *Inorg. Chem.*, 2022, **61**, 19010–19021.
53 R. Nivetha, *et al.*, Cu based Metal Organic Framework (Cu-MOF) for electrocatalytic hydrogen evolution reaction, *Mater. Res. Express*, 2020, **7**, 114001.
54 Z. Dong, *et al.*, High pressure effects on hydrate Cu-BTC investigated by vibrational spectroscopy and synchrotron X-ray diffraction, *RSC Adv.*, 2017, **7**, 55504–55512.
55 A. A. Talin, *et al.*, Tunable Electrical Conductivity in Metal-Organic Framework Thin-Film Devices, *Science*, 2014, **343**, 66–69.
56 S. S. Damasceno, B. B. Dantas, J. Ribeiro-Filho, M. Antônio, D. Araújo, M. Galberto and J. Da Costa, Chemical Properties of Caffeic and Ferulic Acids in Biological System: Implications in Cancer Therapy. A Review, *Curr. Pharm. Des.*, 2017, **23**, 3015–3023.
57 F. Mohseni-Sardari, M. Mazloum-Ardakani, H. Mohammadian-Sarcheshmeh, Z. Alizadeh and S. Houshmand, Enzyme-free glutamate sensor using peony flower-like structure of nickel metal–organic framework/MWCNTs nanocomposite, *Inorg. Chem. Commun.*, 2025, **179**, 114734.
58 S. Ebadi, K. Ghanbari and M. Zahedi-Tabrizi, Development of an electrochemical sensor based on Ni-Bio-MOF and a molecular imprinted polymer for determination of diclofenac: electrochemical and DFT investigations, *RSC Adv.*, 2025, **15**, 16983–16998.
59 B. Dey, *et al.*, Highly sensitive and selective electrochemical sensor for carbendazim detection in fruit juice using novel bi-metallic metal organic framework anchored graphite rod electrode, *Inorg. Chem. Commun.*, 2025, **178**, 114643.
60 Y. Shi, H. Xu, Z. Gu, C. Wang and Y. Du, Sensitive detection of caffeic acid with trifurcate PtCu nanocrystals modified glassy carbon electrode, *Colloids Surf., A*, 2019, **567**, 27–31.

61 T. Shoosri, *et al.*, Bimetallic copper- and nickel-rich Cu–Ni phyllosilicate catalysts for the liquid phase selective hydrogenation of furfural to furfuryl alcohol, *RSC Adv.*, 2024, **14**, 38232–38244.
62 R. Nehru, Y.-F. Hsu and S.-F. Wang, Electrochemical determination of caffeic acid in antioxidant beverages samples via a facile synthesis of carbon/iron-based active electrocatalyst, *Anal. Chim. Acta*, 2020, **1122**, 76–88.
63 H. Hotta, H. Sakamoto, S. Nagano, T. Osakai and Y. Tsujino, Unusually large numbers of electrons for the oxidation of polyphenolic antioxidants, *Biochim. Biophys. Acta, Gen. Subj.*, 2001, **1526**, 159–167.
64 K. B, J. G. Manjunatha, S. M. Osman and N. Ataollahi, Electrochemical polymerized DL-phenylalanine modified carbon nanotube sensor for the selective and sensitive determination of caffeic acid with riboflavin, *Sci. Rep.*, 2024, **14**, 30950.
65 K. Yang, *et al.*, Fabrication of cobalt single-atom catalyst supported on multiwalled carbon nanotubes for enhanced electrochemical sensing of caffeic acid in food samples, *Microchem. J.*, 2025, **213**, 113744.
66 A. Karthika, *et al.*, Green synthesized CaO decorated ternary CaO/g-C_3N_4/PVA nanocomposite modified glassy carbon electrode for enhanced electrochemical detection of caffeic acid, *Sci. Rep.*, 2024, **14**, 28714.
67 M. Sakthivel, *et al.*, Entrapment of bimetallic $CoFeSe_2$ nanosphere on functionalized carbon nanofiber for selective and sensitive electrochemical detection of caffeic acid in wine samples, *Anal. Chim. Acta*, 2018, **1006**, 22–32.
68 T. S. Priya, *et al.*, Non-enzymatic electrochemical detection of caffeic acid in food samples with spinel magnesium cobalt oxide incorporated graphene nanohybrid electrocatalyst, *J. Alloys Compd.*, 2024, **1002**, 175335.